J. Fluid Mech. (1987), *vol.* 181, *pp.* 265–291
Printed in Great Britain

Experimental and theoretical investigation of nonlinear sloshing waves in a rectangular channel

By E. KIT, L. SHEMER AND T. MILOH
Faculty of Engineering, Tel-Aviv University, Tel-Aviv 69978, Israel

(Received 29 August 1986)

Experimental and theoretical studies of sloshing waves in a rectangular channel in the vicinity of the second cutoff frequency are presented. The experiments were performed in a wave tank which is 1.2 m wide, 18 m long and 0.9 m deep. Sloshing waves were generated by a computer-controlled segmented wavemaker consisting of four independent modules. A sharp transition between two wave patterns, which exhibited hysteresis-type behaviour, was observed. At lower forcing frequencies a steady wave regime was obtained, while at higher frequencies modulation on a long timescale appeared. At stronger forcing, solitons were generated periodically at the wavemaker and then propagated away with a seemingly constant velocity. Experimental results are compared with numerical solutions of the appropriate nonlinear Schrödinger equation, a derivation of which is also presented. The importance of dissipation on the physical processes of wave evolution is discussed, and a simple dissipative model is suggested and incorporated in the governing equations.

1. Introduction

It is well known (e.g. Barnard, Mahony & Pritchard 1977, hereinafter referred to as BMP; Miloh 1987) that resonant waves with crests parallel to the channel walls and with wavelengths $\lambda = (2b)/n$, n being an integer representing the mode number, may appear in a semi-infinite channel of depth h and width b. These waves may be generated by a wavemaker, whose instantaneous shape in the direction normal to the channel walls has a typical wavelength λ, and which operates at frequency close to the cutoff value defined by $\omega^2 = (2g\pi/\lambda)\tanh(2\pi/\lambda)h$. Waves formed in this manner are usually referred to as 'sloshing waves'. An alternative way of generating similar waves is parametric excitation by a plane wavemaker at subharmonic frequency, Garrett (1970), Barnard & Pritchard (1972), Lichter & Shemer 1986). These waves are known as 'cross-waves'. Linear theory of sloshing waves, given e.g. in Wehausen (1974), fails to describe correctly the wave response in the vicinity of the cutoff frequencies (Shemer, Kit & Miloh 1987), since it yields infinite amplitudes at these frequencies. In order to account for the finite wave amplitude observed experimentally at the cutoff frequency, nonlinear effects have to be considered in the theoretical model, although dissipation can become crucial under certain circumstances.

The most extensive experimental work reported on sloshing waves is due to BMP. They have performed measurements covering a wide range of forcing amplitudes in the vicinity of the first cutoff frequency by using a pointer-type wave gauge. BMP have observed that two distinct steady wave patterns may exist in the channel at identical forcing conditions. In some experiments the maximum of the wave height distribution along the channel was found to be shifted downwards from the wavemaker. A similar result was also reported by Barnard & Pritchard (1972) in their experiments on cross-waves. Miles (1985) suggested that this type of distribution may be interpreted as a trapped soliton.

A steady soliton-like solution was observed experimentally by Wu, Keolian & Rudnick (1984). An analysis of this non-propagating soliton was made by Larraza & Putterman (1984) by employing the nonlinear Schrödinger (NLS) equation and by Miles (1984).

A consistent to third-order derivation of the nonlinear Schrödinger equation for the propagation of an acoustic wave in a duct, including a wavemaker-like forcing, was given by Aranha, Yue & Mei (1982). Their numerical solutions revealed that in the case which is analogous to deep water in the channel, no steady solution of the NLS equation can be obtained. The solution of an initial boundary-value problem gave a wave pattern which can be decomposed into two parts: an unsteady decaying wave adjacent to the wavemaker, and a single solition which propagates away from the wavemaker. The unsteady character of the solution obtained numerically by Aranha *et al.* (1982) is in contrast with the steady distribution observed experimentally by BMP.

This contradiction between the only experimental results known to us on sloshing waves and the numerical predictions, triggered our interest in this problem and was the main motivation for the present study. We decided to take advantage of our considerably larger wave tank, compared with the one used by BMP, which was about 30 cm wide.

In a bigger facility one can generally expect lower dissipation rates. It is plausible to assume that the strong dissipation in BMP experiments is at least partially responsible for the evident discrepancy between their reported results and the numerical predictions of Aranha *et al.* By using our modular wavemaker it is possible to generate both the first and the second modes of sloshing waves. Our present experiments were restricted to the second mode, where detailed computer-based measurements of waveforms in the vicinity of the second cutoff frequency were performed. The experimental results are supplemented by a derivation of the nonlinear Schrödinger equation which is found to be appropriate for sloshing waves. Numerical solutions of this equation are also presented.

2. Theory

Consider a semi-infinite rectangular wave tank of width b and water depth h equipped with a wavemaker situated at $x=0$. The undisturbed free surface is $z=0$ (with z pointing vertically upward), $z=-h$ is the bottom and the two parallel channel walls lie at $y=0$ and $y=b$. All variables are now rendered dimensionless using b as a lengthscale and $(b/g)^{\frac{1}{2}}$ as a timescale. The governing equation and the free-surface boundary conditions, relating the induced velocity potential $\phi(x,y,z,t)$ and the resulting free-surface elevation $\eta(x,y,t)$, are as follows:

$$\nabla^2\phi = 0 \quad (0<y<1;\ -h<z<\eta(x,y,t)) \tag{2.1}$$

$$\left.\begin{aligned} \eta_t+\phi_x\eta_x+\phi_y\eta_y &= \phi_z \quad (2.2a)\\ \phi_t+\eta+\tfrac{1}{2}\nabla\phi\cdot\nabla\phi &= 0 \quad (2.2b)\end{aligned}\right\} \quad (z=\eta(x,y,t)).$$

This should be supplemented by the boundary conditions on the channel walls:

$$\phi_y = 0 \quad (y = 0, 1), \tag{2.3a}$$

$$\phi_z = 0 \quad (z = -h). \tag{2.3b}$$

Eliminating the free-surface displacement η from (2.2) and (2.3) and using Taylor expansion about $z = 0$, yields the following relationship correct to third order (Newman 1977):

$$\begin{aligned}\phi_{tt}+\phi_z+2\nabla\phi\,\nabla\phi_t+\tfrac{1}{2}\nabla\phi\cdot\nabla(\nabla\phi\cdot\nabla\phi)-\phi_t(\phi_{tt}+\phi_z+2\nabla\phi\,\nabla\phi_t)_z \\ -(-\phi_t\,\phi_{zt}+\tfrac{1}{2}\nabla\phi\cdot\nabla\phi)\,(\phi_{tt}+\phi_z)_z+\tfrac{1}{2}\phi_t^2(\phi_{tt}+\phi_z)_{zz} = 0.\end{aligned} \tag{2.4}$$

The boundary condition at the wavemaker is

$$\phi_x = \epsilon(\xi_t+\phi_y\,\xi_y+\phi_z\,\xi_z) \quad \text{at } x = s\xi(y,z,t) = \tfrac{1}{2}sf(y,z)\,(\mathrm{e}^{-\mathrm{i}\Omega t}+\text{c.c.}), \tag{2.5}$$

where ϵ is a small parameter related to the amplitude of the wavemaker s, c.c. denotes complex conjugate and the 4-segment wavemaker shape $f(y,z)$ is given by

$$f(y,z) = \begin{cases} \left(1+\dfrac{z}{h}\right) & (0 < y < \tfrac{1}{4}b, \tfrac{3}{4}b < y < b), \\ -\left(1+\dfrac{z}{h}\right) & (\tfrac{1}{4}b < y < \tfrac{3}{4}b), \end{cases} \tag{2.6}$$

in order to obtain the second sloshing mode with zero net displacement. The forcing frequency Ω is related to the wavenumber k by the linear dispersion relation

$$\Omega^2 = k \tanh kh. \tag{2.7}$$

The condition at infinity is

$$\phi \rightarrow 0 \quad \text{as } x \rightarrow \infty, \tag{2.8}$$

and the initial condition is given by

$$\phi(x,y,z,0) = \phi_0(x,y,z), \tag{2.9}$$

where ϕ_0 is a known function. The linear solution of (2.1) with boundary conditions (2.2), (2.3) is given by Wehausen (1974) and Shemer *et al.* (1987)

$$\phi = \epsilon \cos k_2 y \frac{\cosh k_2(z+h)}{\cosh k_2 h}(C_2 \exp(-\mathrm{i}\Omega t)+\text{c.c.}), \tag{2.10}$$

where $k_2 = 2\pi$ is the wavenumber at the second cutoff frequency $\omega_2 = (k_2 \tanh k_2 h)^{\frac{1}{2}}$; C_2 is given by

$$C_2 = -\frac{\mathrm{i}f_2}{(k^2-k_2^2)^{\frac{1}{2}}} \exp(\mathrm{i}(k^2-k_2^2)^{\frac{1}{2}}x) \quad \text{for } k > k_2, \tag{2.11a}$$

$$C_2 = -\frac{f_2}{(k_2^2-k^2)^{\frac{1}{2}}} \exp(-(k_2^2-k^2)^{\frac{1}{2}}x) \quad \text{for } k < k_2, \tag{2.11b}$$

and

$$f_2 = \int_0^1 \mathrm{d}y \int_{-h}^0 \mathrm{d}z\, f(y,z) \cos k_2 y \frac{\cosh k_2(z+h)}{\cosh k_2 h}. \tag{2.12}$$

The parasitic modes related to the shape of the wavemaker can be disregarded in the vicinity of cutoff frequencies (Shemer *et al.* 1987). The value of f_2 obtained from (2.12) for the geometry of our wavemaker is $f_2 = 1.616$.

Adopting the approach used by Aranha *et al.* (1982) and using the dispersion relation (2.7), the variation of $C_2 \exp(-\mathrm{i}\Omega t)$ around ω_2 can be rewritten as

$$\mathrm{e}^{-\mathrm{i}\omega_2 t} \exp\left[\mathrm{i}\left(\surd 2 \frac{\omega_2}{\tanh k_2 h}(\Omega^2-\omega_2^2)^{\frac{1}{2}} x - \frac{\mathrm{i}(\Omega^2-\omega_2^2)\,t}{2\omega_2}\right)\right], \quad \Omega > \omega_2, \tag{2.13a}$$

$$\mathrm{e}^{-\mathrm{i}\omega_2 t} \exp\left[-\left(\surd 2 \frac{\omega_2}{\tanh k_2 h}(\omega_2^2-\Omega)^{\frac{1}{2}} x - \frac{\mathrm{i}(\Omega^2-\omega_2^2)\,t}{2\omega_2}\right)\right], \quad \Omega < \omega_2. \tag{2.13b}$$

Equations (2.13) in the immediate vicinity of the second cutoff frequency ω_2 define slow modulations in x and t. The detuning parameter λ and slow variables X and τ are now introduced

$$\lambda = \frac{\Omega^2-\omega_2^2}{\epsilon} \approx \frac{2\omega_2(\Omega-\omega_2)}{\epsilon}, \quad X = \epsilon^{\frac{1}{2}} x, \quad \tau = \frac{\epsilon t}{2\omega_2}. \tag{2.14}$$

This particular ordering between physical and slow variables, as well as the relationship between the forcing frequency Ω and the cutoff frequency ω_2, was chosen so as to eliminate secular first harmonic terms in the third order (Aranha *et al.* 1982).

A three-term expansion of ϕ can be represented as

$$\phi = \epsilon^{\frac{1}{2}}\phi_1 + \epsilon\phi_2 + \epsilon^{\frac{3}{2}}\phi_3 + O(\epsilon^2). \tag{2.15}$$

We look for solutions of (2.1) with boundary conditions (2.2) and (2.3), valid to $\epsilon^{\frac{3}{2}}$. The fast-time independent (DC) terms will be disregarded in the derivation and referred to later.

Order $\epsilon^{\frac{1}{2}}$

$$\Delta\phi_1 = 0 \quad \text{for } 0 < y < 1; \quad -h < z < 0, \tag{2.16}$$

$$\phi_{1_{tt}} + \phi_{1_z} = 0 \quad \text{at } z = 0, \tag{2.17}$$

$$\phi_{1_y} = 0 \quad \text{at } y = 0, 1; \quad \phi_{1_z} = 0 \quad \text{at } z = -h. \tag{2.18}$$

The solution of (2.16) with boundary conditions (2.17), (2.18) is given by

$$\phi_1 = \cos k_2 y \frac{\cosh k_2(z+h)}{\cosh k_2 h}(C(X,\tau)\,\mathrm{e}^{-\mathrm{i}\Omega t} + \text{c.c.}). \tag{2.19}$$

The boundary condition at the wavemaker (2.5) can now be rewritten

$$\epsilon \left.\frac{\partial C}{\partial X}\right|_{X=0} = -\tfrac{1}{2}\mathrm{i}\Omega f_2 s; \tag{2.20}$$

thus

$$\left.\frac{\partial C}{\partial X}\right|_{X=0} = -\mathrm{i}\Omega, \tag{2.21}$$

and the relation between ϵ and the stroke of the wavemaker s is obtained,

$$\epsilon = f_2 \tfrac{1}{2} s. \tag{2.22}$$

Order ϵ

$$\Delta\phi_2 = 0. \tag{2.23}$$

Denoting $T = \tanh k_2 h$, substituting (2.19) into (2.4) and retaining terms up to the second order yields

$$\phi_{2_{tt}} + \phi_{2_z} = \Omega k_2^2 [\tfrac{1}{2}(1+3T^2) + \tfrac{3}{2}(T^2-1)\cos 2k_2 y]\,(\mathrm{i}C^2\,\mathrm{e}^{-2\mathrm{i}\Omega t} + \text{c.c.}), \tag{2.24}$$

with the boundary conditions

$$\phi_{2_y} = 0 \quad \text{at } y = 0; 1, \quad \phi_{2_z} = 0 \quad \text{at } z = -h. \tag{2.25}$$

The solution is given by

$$\phi_2 = k_2^2 \left[-\frac{1+3T^2}{8\Omega} + \frac{3}{8}\frac{1-T^4}{T^2\Omega} \cos k_2 y \frac{\cosh 2k_2(z+h)}{\cosh 2k_2 h} \right] (\mathrm{i}C^2\, \mathrm{e}^{-2\mathrm{i}\Omega t} + \text{c.c.}). \tag{2.26}$$

Order $\epsilon^{\frac{3}{2}}$

The governing equation,

$$\Delta\phi_3 = -\frac{\partial^2 \phi_1}{\partial X^2} = -\cos k_2 y \frac{\cosh k_2(z+h)}{\cosh k_2 h} \left(\frac{\partial^2 C}{\partial X^2}\, \mathrm{e}^{-\mathrm{i}\Omega t} + \text{c.c.} \right). \tag{2.27}$$

Boundary conditions

$$\begin{aligned} \phi_{3_{tt}} + \phi_{3_z} = {} & q_{31}(|C|^2 C\, \mathrm{e}^{-\mathrm{i}\Omega t} + \text{c.c.}) + q_{33}(C^3\, \mathrm{e}^{-3\mathrm{i}\Omega t} + \text{c.c.}) \\ & - \left[\left(\mathrm{i}\frac{\partial C}{\partial \tau} + \lambda C \right) \mathrm{e}^{-\mathrm{i}\Omega t} + \text{c.c.} \right] \cos k_2 y \quad \text{at } z = 0, \end{aligned} \tag{2.28}$$

where

$$\begin{aligned} q_{31} = -k_2^4 \Bigg[& \frac{3(1-T^2)}{2T^2} \sin k_2 y \sin 2k_2 y + \frac{3(1-T^2)^3}{4T^2} \cos k_2 y \cos 2k_2 y \\ & + \frac{-T^4+4T^2-5}{4} \cos k_2 y + \tfrac{1}{2}(1-T^2)(3-T^2) \cos^3 k_2 y \Bigg], \end{aligned} \tag{2.29}$$

$$\phi_{3_y} = 0 \quad \text{at } y = 0, 1; \quad \phi_{3_z} = 0 \quad \text{at } z = -h. \tag{2.30}$$

The necessary condition for solvability of inhomogeneous problem (2.27)–(2.30), which may be obtained using the Green's theorem (see, e.g. Stakgold 1979), yields

$$\mathrm{i}\frac{\partial C}{\partial \tau} + c_g^2 \frac{\partial^2 C}{\partial X^2} + \lambda C + K|C|^2 C = 0, \tag{2.31}$$

where

$$c_g^2 = \frac{T + k_2 h(1-T^2)}{2k_2}, \tag{2.32}$$

and

$$K = \tfrac{1}{8}k_2^4 \left(6T^4 - 5T^2 + 16 - \frac{9}{T^2} \right). \tag{2.33}$$

For deep water ($k_2 h \rightarrow \infty, T = 1$),

$$K = k_2^4. \tag{2.34}$$

The deep-water approximation (2.34) was found to hold in our experimental facility, where $k_2 h = \pi$.

The expression (2.33), obtained here for the nonlinear term, is in agreement with the one given by Larraza & Putterman (1984) and differs from the coefficient of Tadjbakhsh & Keller (1960) and Miles (1976):

$$K = \tfrac{1}{8}k^4 \left(2T^4 + 3T^2 + 12 - \frac{9}{T^2} \right). \tag{2.35}$$

As was pointed out by Larraza & Putterman, this discrepancy stems from the difference in the effective mean water depth. In our derivation, as well as in that of Larraza & Putterman, mean water depth was assumed constant. The alternative expression (2.35) can be obtained from (2.33) by realizing that the nonlinear term causes a change in the mean water depth. This change is given up to second order by

$$\eta_0 = \tfrac{1}{2}[(\phi_t)^2_z - (\nabla\phi)^2] \tag{2.36}$$

(Larraza & Putterman 1984). When this shift in the mean water depth is incorporated in the dispersion relation, one obtains the amplitude-dependent resonant frequency

$$\omega^2_2 = \omega^2_2(h) + \tfrac{1}{2}(1-T^2)^2\, k^4_2\, \phi^4. \tag{2.37}$$

The substitution of (2.37) into (2.14) and (2.31) yields the value of K, which corresponds to (2.35).

In the case of an infinite channel, the expression (2.35) should be used, since then the local change in the mean water depth actually takes place and does not influence the mean water level in the whole channel. On the other hand, when the channel is of finite length comparable with the length of the disturbance, no local change in the mean water depth can occur due to the total volume conservation, and hence (2.33) is valid.

It is convenient to renormalize the variables and the coefficients of (2.31) in the following way:

$$\hat{\lambda} = \frac{2\lambda}{K}, \quad \hat{X} = \left(\frac{K}{2c^2_g}\right)^{\frac{1}{2}}, \quad \hat{\tau} = \tfrac{1}{2}K\tau, \tag{2.38}$$

so that the nonlinear Schrödinger equation (2.31) can now be rewritten in its standard form:

$$\mathrm{i}\frac{\partial C}{\partial \hat{\tau}} + \frac{\partial^2 C}{\partial \hat{X}^2} + \hat{\lambda} C + 2|C|^2 C = 0. \tag{2.39}$$

In order to compare the theoretical results with the experimental data, the relation between the renormalized dimensionless quantities and the corresponding physical values is necessary. Using (2.38) and (2.14) for the deep-water case ($K = (2\pi)^4$; $c^2_g = 1/4\pi$), one obtains

$$\hat{X} = (2\pi)^{\frac{5}{2}}\, \hat{\epsilon}^{\frac{1}{2}} \frac{x}{b}, \quad \hat{\tau} = 4\pi^4 \hat{\epsilon} \frac{\Omega t}{2\pi}, \quad \hat{\lambda} = \frac{4\omega_2(\Omega - \omega_2)}{(2\pi)^4\, \hat{\epsilon}} \frac{b}{g}. \tag{2.40}$$

The boundary condition at the wavemaker (2.21) is now replaced by

$$\left.\frac{\partial C}{\partial \hat{X}}\right|_{\hat{X}=0} = -\mathrm{i}, \tag{2.41}$$

so that the normalized value of $\hat{\epsilon}$ is related to the wavemaker stroke s by

$$\hat{\epsilon} = \frac{f_2}{8\pi^2} \frac{s}{b}. \tag{2.42}$$

The symbol ^ will be omitted from here on.

3. Numerical solutions

Equation (2.39) is identical to the NLS equation solved by Aranha *et al.* The numerical scheme presented in their paper has been adopted in the present work. Equation (2.39) with the boundary condition (2.41) and zero initial condition was solved numerically using a semi-implicit Crank–Nicolson-type scheme and by employing explicit estimation of the nonlinear term. Some calculations were also

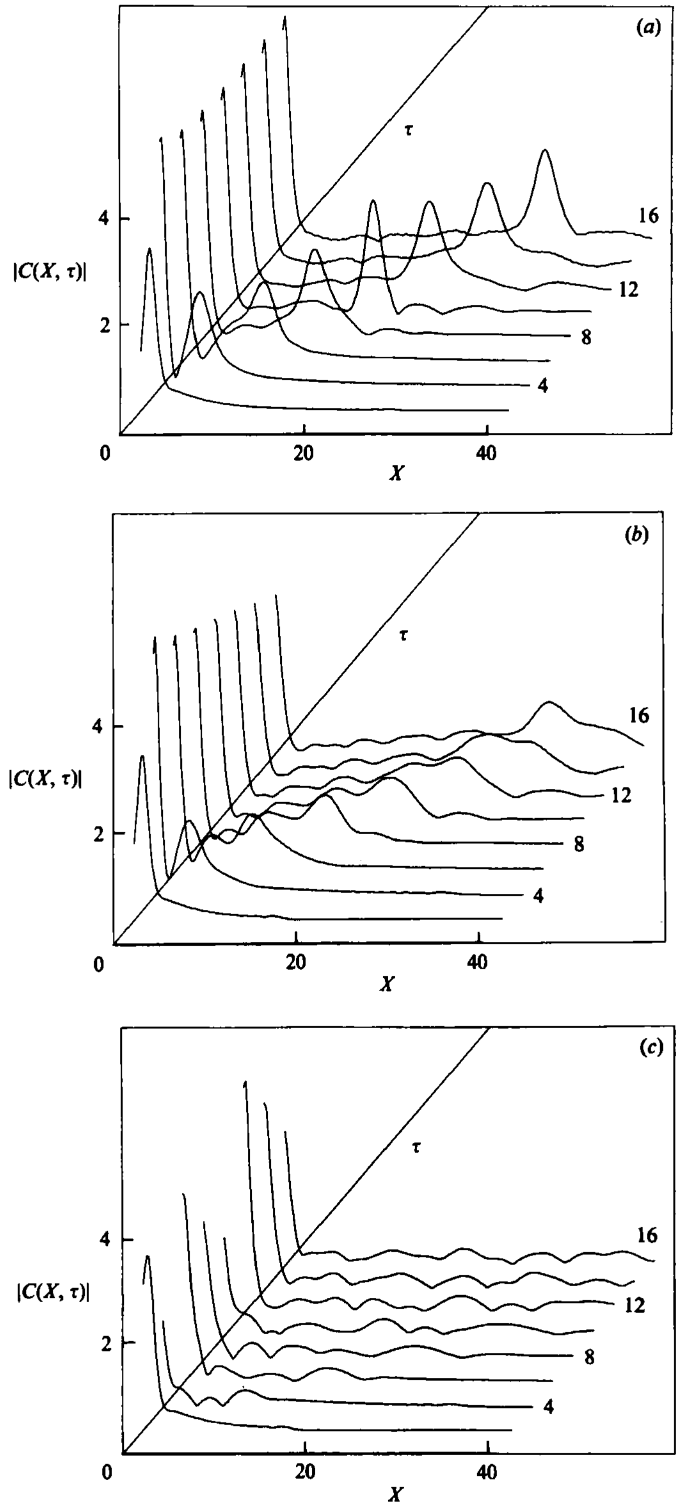

Figure 1. Space–time evolution of $|C(X, T)|$ for the inviscid case; (*a*) $\lambda = -0.1$; (*b*) $\lambda = -0.2$; (*c*) $\lambda = -0.5$.

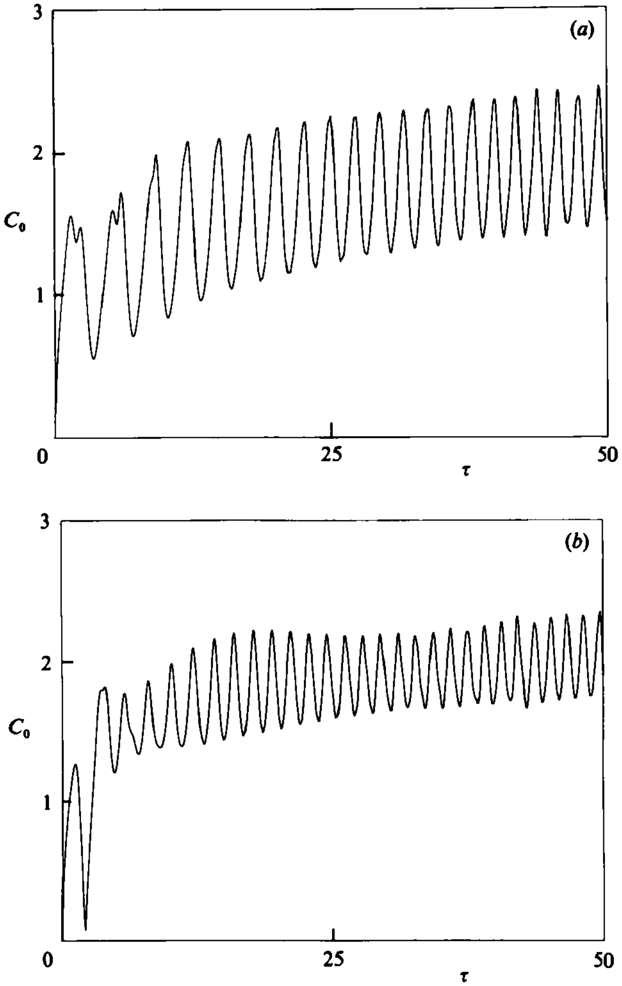

FIGURE 2. Time evolution of the wave amplitude at the wavemaker; (*a*) $\lambda = -0.5$; (*b*) $\lambda = -0.1$.

performed using the numerical scheme of Stiassnie & Kroszynski (1982) with iterative estimation of the nonlinear term. Both methods gave very similar results. The step sizes were smaller than those checked by Aranha *et al.* (i.e. $\Delta X \leqslant 0.2$; $\Delta\tau \leqslant 0.025$). In most of the runs presented here, we chose $\Delta X = 0.1$ and $\Delta\tau = 0.005$. Substitution of the length of the channel $L = 18$ m into (2.40) gives for the maximum amplitude of forcing the renormalized value of L less than 20. In order to eliminate the influence of the far end of the channel, the calculations were performed for $0 \leqslant X \leqslant 100$, which is equivalent to a channel substantially longer than the present one. The results, however, are presented only for $X \leqslant 40$.

Figure 1 (*a*) shows the space–time evolution of $|C(X, \tau)|$ for $\lambda = -0.1$. A propagating soliton, similar to the one found by Aranha *et al.* for positive and zero values of the detuning parameter λ, was obtained. Once generated, the soliton propagates with a constant velocity down the channel. The non-dimensional propagation velocity estimated from figure 1 (*a*) is about 2, in agreement with the result obtained by Aranha *et al.* for $\lambda = 0$. The height of the soliton increases initially (up to about

$\tau = 10$), and then decreases again with some of the energy apparently transferred to the background waves at $\tau > 10$.

Similar calculations which were performed for $\lambda = -0.2$, gave a much flatter soliton with a substantially lower height. However, it is important to note that the propagation velocity remains essentially unchanged compared with that measured from figure 1(*a*). For $\lambda = -0.5$, no soliton-like solution, was obtained, and the solution resembles the reported results of Aranha *et al.* for $\lambda = -1$ and $\lambda = -2$.

Since the nonlinear term coefficient in (2.39) is positive, no steady solutions can be expected for $\lambda = 0$ (Aranha *et al.*). The present calculations show that the steady state is never reached for all values of λ employed. Figure 2 shows the variation of $C_0(\tau) = |C(0, \tau)|$ for $\lambda = -0.5$ (figure 2*a*) and for $\lambda = 0.1$ (figure 2*b*). While the results are qualitatively similar, the oscillations of the wave amplitude at the wavemaker have both amplitudes and frequencies which depend strongly on λ. The amplitude behaviour in the initial stage of evolution is also notably different.

4. Experimental procedure

Experiments were performed in a wave tank which is 18 m long, 1.2 m wide, and 0.9 m deep, and filled to a mean water level of 0.6 m. Waves were generated by a modular paddle-type wavemaker which consisted of four independent sections. A beach for wave energy absorption was placed at the far end of the tank. The detailed description of the experimental facility is given in Shemer *et al.* (1987).

A stable wavemaker frequency with the possibility of fine tuning is indispensable for obtaining accurate and repeatable results in the close vicinity of the cutoff frequency, for low absolute values of the detuning parameter λ. These features are extremely important since the most intriguing nonlinear phenomena occur in a very narrow frequency band and depend critically on previous history. For this reason it was decided to operate the wavemaker using a 1 MHz quartz clock of a PDP 11/23 minicomputer. A total of 32 data points were used to emulate the sinusoidal signal. The output of the D/A converter was low-pass filtered using a Krohn–Hite filter. In this way a period resolution of 32 μs was obtained. Since the forcing period for the second cutoff frequency, where the measurements were made, is about 880 ms, the tuning accuracy $(\Delta\Omega)/\Omega$ which could be attained was as good as 3.6×10^{-5}. In order to obtain a second-mode sloshing wave with a zero net displacement, and thus to eliminate the contamination of the wave field by a plane propagating wave, all wavemaker sections were operated at identical amplitudes with a 180° phase shift between the two inner and the two outer wavemaker segments.

The instantaneous position of each wavemaker section could be monitored using the output signals of the position potentiometers. The instantaneous surface elevation of the induced wavefield was measured by four conductance-type wave height gauges which were located along the centreline of the channel. The gauges were placed on a bar and could be moved by a carriage along the tank.

The outputs of 4 wave gauges, 4 wavemaker position potentiometers, and the forcing signal which served as phase reference, were sampled instantaneously using an A/D converter of the same minicomputer. All information was recorded on a magnetic tape for further processing. This procedure enabled us to perform long-time measurements. At a later stage the recorded time series for each data channel were phase-averaged and the corresponding amplitudes and phases were obtained from these phase-averaged signals using the Fourier transform. The data processing procedure is given in detail in Shemer *et al.* (1987).

Experiments were performed at 3 values of the wavemaker stroke at the mean water level: 0.25 cm, 0.35 cm and 0.49 cm, corresponding to the normalized dimensionless forcing amplitudes, defined by (2.42), of $\epsilon = 0.42 \times 10^{-4}$, $\epsilon = 0.60 \times 10^{-4}$ and $\epsilon = 0.83 \times 10^{-4}$, respectively. These values of ϵ were used to normalize the experimentally measured quantities according to (2.40).

5. Experimental results

5.1. *Wide frequency range*

The general behaviour of sloshing waves for frequencies away from the cutoff, is described reasonably well by the linear theory (Shemer *et al.* 1987). In the present work we are interested in the sloshing-wave response in the close vicinity of the cutoff frequency, where nonlinear effects become dominant. Linear theory suggests the existence of two distinct wave regimes in the channel. Below the cutoff frequency, one can expect a decaying wave field whereas a radiating wave is generated at frequencies above the cutoff. The critical frequency range, where transition from one wave regime to another occurs, is amplitude-dependent and down-shifted relative to the linear cutoff value, (Penney & Price 1952). In view of the fact that the exact boundary conditions on the beach at the far end of the tank are not well defined, it was decided to restrict the experiments to conditions where no influence of the far end can be observed and the water close to the beach remains practically still. Detailed waveform measurements were thus performed mainly at frequencies below the cutoff value where the wave amplitude decays along the channel.

In order to isolate the frequency range where most interesting nonlinear phenomena can be observed, measurements were first performed covering a relatively wide frequency region. Figure 3 show the wavenumber dependence of the amplitude a, (figure 3a), and the phase angle relative to the phase of central sections of the wavemaker, ϕ, (figure 3b), measured by the wave gauge located close to the wavemaker ($x = 11$ cm, which corresponds to the normalized dimensionless $X = 0.070$) at intermediate amplitude of forcing ($\epsilon = 0.60 \times 10^{-4}$).

Linear theory predicts a 180° phase shift between the amplitudes of the wavemaker and the surface elevation for the decaying regime and a 90° phase shift for the radiating wave. Figure 3(b) indicates that the linear limit is approached at a relatively low frequency ($kb/\pi \leqslant 1.8$, where k is the dimensional wavenumber, corresponding to the values of the detuning parameter $\lambda \leqslant -13$). Increasing the frequency of the wavemaker results in a decrease of the phase shift ϕ. It is important to note that the energy rate introduced into the system by the wavemaker when operating at frequency Ω and with a stroke s, is proportional to the product $\Omega s \cdot a \sin\phi$. The deviation of ϕ from 180° in the vicinity of the resonance clearly indicates that there exists an energy feed mechanism into the wave field. Contrary to the radiating mode, no energy transfer to infinity occurs in the decaying regime, thus energy dissipation, being the only possible energy sink, plays an important role in this range of frequencies.

The wave amplitude attains a maximum at $kb/\pi = 1.95\,(\lambda = -3)$, and then decreases. It is interesting to note that at approximately the same value of kb/π the phase shift ϕ crosses the 90° line and thus the energy flow exhibits there a pronounced maximum.

At $kb/\pi \approx 1.991$ ($\lambda \approx -0.60$), a dramatic transition in the wave-field pattern is observed which manifests itself in figure 3 in the form of a jump in both amplitude

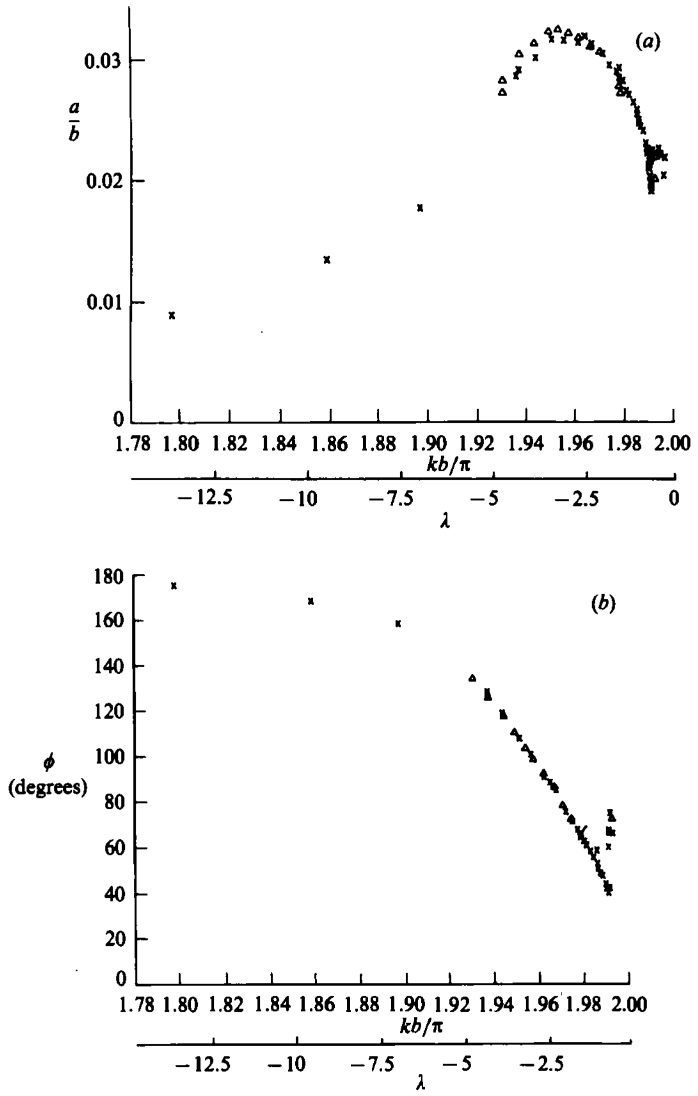

FIGURE 3. The dependence of (*a*) wave amplitudes and (*b*) wave phase angles on wavenumber. Forcing amplitude $\epsilon = 0.60 \times 10^{-4}$, probe location $x = 11$ cm, $X = 0.070$.

and phase angle. Observation of the wave field in the tank suggests that a wave pattern of radiating nature is generated. The increase in the phase angle ϕ, which now approaches the value of 90°, supports this suggestion. The detailed investigation of the transition process, is one of the main goals of the present work.

5.2. *Phase distributions*

Most interesting nonlinear phenomena are to be expected in the transition region where the history of the wave field may be of importance. A possibility of the existence of two distinct wave patterns at identical forcing conditions, was first observed by BMP. Examples displaying wave phase angles in the vicinity of the wavemaker ($x = 11$ cm) for three amplitudes of forcing, as a function of frequency,

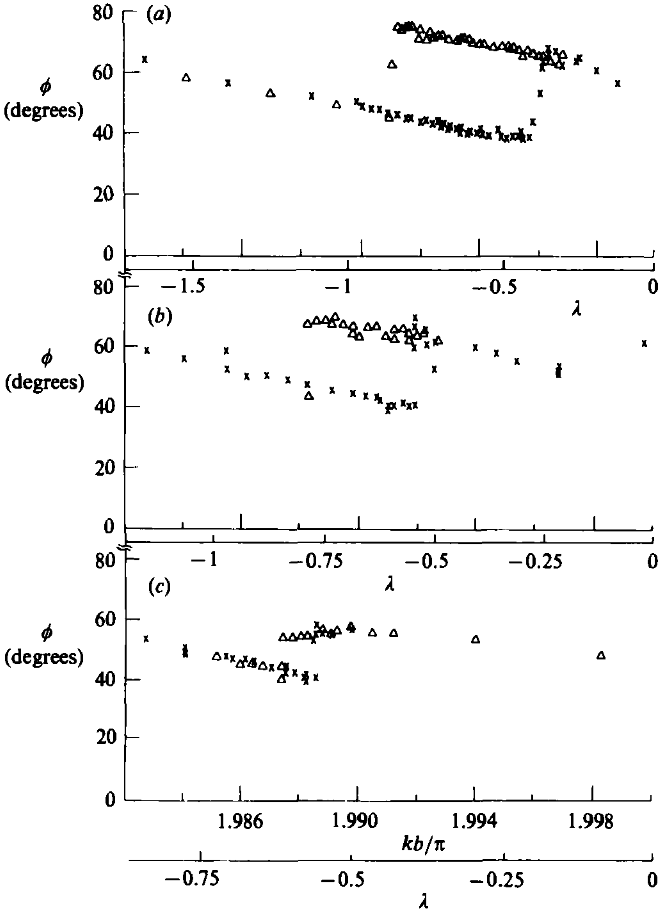

FIGURE 4. The dependence of phase angles of probe located at $x = 11$ cm on wavenumber; ×, for increasing frequency; △, for decreasing frequency. Forcing amplitude: (a) $\epsilon = 0.42\times10^{-4}$; (b) $\epsilon = 0.60\times10^{-4}$; (c) $\epsilon = 0.83\times10^{-4}$.

are presented in figure 4. In order to obtain these distributions, special care was taken to vary the forcing frequency monotonically. This could be achieved due to the special features provided by the computer control of the wavemaker.

Two distinct modes may be observed at identical forcing conditions. One mode is obtained when the forcing frequency is increased monotonically from relatively low values, until a sudden increase in the phase angle occurs, with corresponding radical change in the whole wave field. This wave pattern, which is characterized in figure 4 by relatively low values of the phase angles, will be called here a 'decaying' mode. The second mode, with higher values of the phase angles, will be denoted as a 'radiating' mode. This notation represents the generalization of the linear theory, where the transition between the two modes occurs at the cutoff frequency. The sharp transition between the modes, on one hand, and the gradual change in the wave parameters beyond the transition region, on the other hand, seem to justify this notation. One has to keep in mind, though, that in the transition region the 'decaying' and the 'radiating' modes are quite different from their linear counterparts, where the phase shifts are 180° and 90°, respectively.

The hysteresis-type behaviour is evident for all three forcing amplitudes shown in

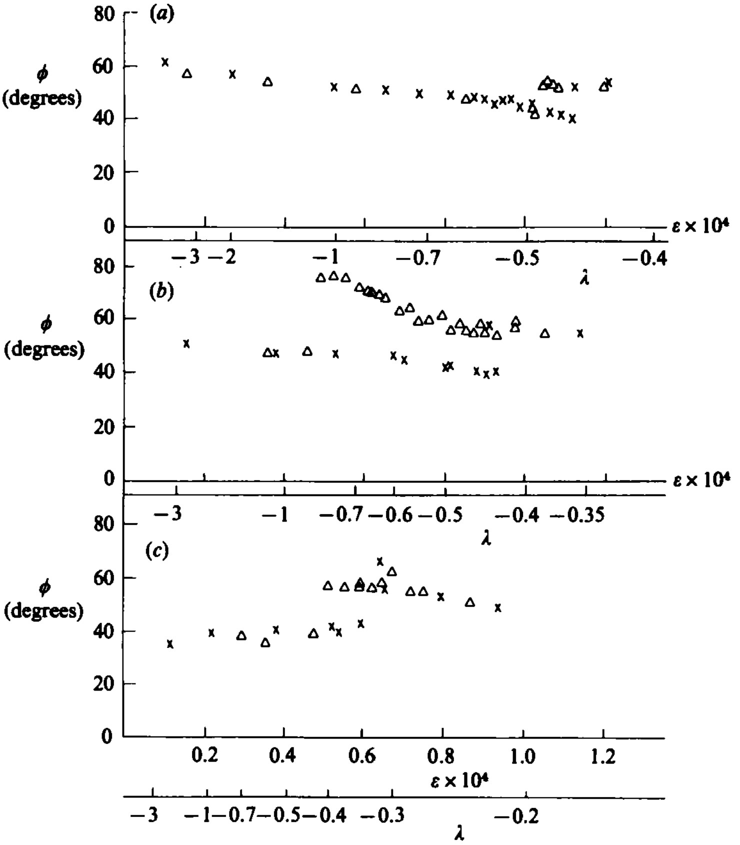

FIGURE 5. The dependence of wave-phase angle ϕ on amplitude of forcing for $x = 11$ cm; (*a*) $kb/\pi = 1.9869$, (*b*) $kb/\pi = 1.9900$, and $kb/\pi = 1.9950$; ×, increasing amplitude; △, decreasing amplitude.

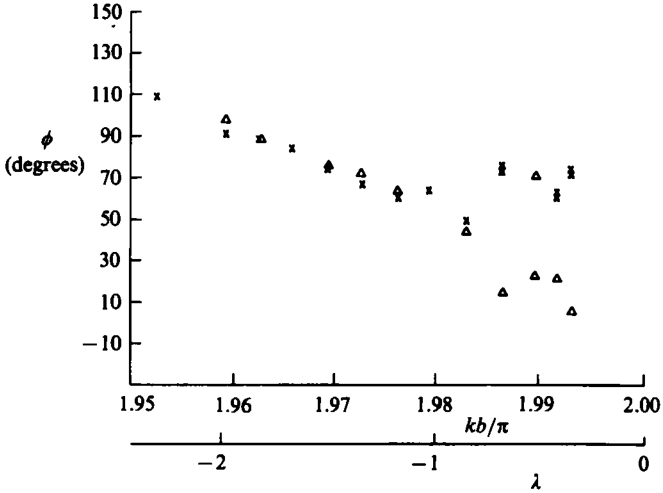

FIGURE 6. The dependence of phase angles of probes located at ×, 11 cm, $X = 0.083$; and △, 160 cm, $X = 1.20$, on wavenumber, forcing amplitude $\epsilon = 0.83 \times 10^{-4}$.

figure 4. The transition from the 'decaying' to the 'radiating' mode occurs at frequencies which are slightly higher than those at which a reverse transition is observed. Generally speaking, the transition region is shifted towards lower frequencies with increasing amplitudes. Stronger forcing also causes the hysteresis loop to become narrower. It is interesting to note that close to the transition point the phase angle of the 'decaying' mode, in all three cases, attains practically the same value of approximately 40°, while the phase of the 'radiating' mode decreases significantly with increasing amplitude.

In figure 4 the hysteresis loop was obtained by keeping the forcing amplitude constant. The same phenomenon could be obtained by varying the forcing amplitude at a constant frequency (figure 5). At the lowest wavemaker frequency (figure 5*a*), very high amplitudes and thus strong nonlinear effects, are necessary in order to generate a 'radiating' regime. On the contrary, at high frequencies (figure 5*c*), the 'decaying' mode can be observed only for very low forcing amplitudes. At an intermediate frequency (figure 5*b*), a wide hysteresis loop was obtained. One notices that here again the transition from 'decaying' to 'radiating' mode, for all values of forcing, occurs when the phase shift is about 40°.

Figures 4 and 5 illustrated the transition between the 'decaying' and the 'radiating' modes by showing the frequency dependence of the surface elevation phase angle in the vicinity of the wavemaker. This transition at forcing amplitude $\epsilon = 0.83\times 10^{-4}$ is shown in figure 6 from a different point of view. The phase angles relative to the wavemaker are shown here for two probes located at 11 cm and 160 cm (corresponding to a dimensionless renormalized $X = 0.083$ and $X = 1.20$, respectively). One can immediately see that for $kb/\pi < 1.986$ ($\lambda < -0.68$), the phase angles are identical, as expected for a standing wave. The transition at this higher amplitude occurs at a lower value of kb/π than in figure 3. The wave field beyond transition is characterized by an increased value of ϕ close to the wavemaker, similar to the results displayed in figure 3(*b*). On the other hand, the phase angle at the downstream position continues to decrease. Significant phase differences measured at different locations indicate that energy is propagating along the channel, as it is expected in the radiating wave regime. This observation provides an additional justification for the accepted notation of the wave modes. It is observed in the experiments that due to dissipation the amplitude of the propagating wave decays well before the beach.

5.3. *Amplitude distributions along the channel*

Examples displaying two different wave amplitude distributions along the channel at the same amplitudes and frequencies of forcing are presented in figure 7. In this figure, distribution I was obtained when the desired frequency was approached from below, while distribution II represents the case where the same frequency was approached from above. Curves I represent therefore the 'decaying' wave regime. At a lower frequency, the wave amplitude decays monotonically (although the decay is not exponential and an inflexion point in the longitudinal wave amplitude distribution is clearly seen). The slight increase in the frequency, which amounts to an increase in kb/π by 0.06 %, results in a qualitatively different distribution where the maximum amplitude was found to be detached from the wavemaker. The wave amplitudes at this frequency, after attaining a maximum, decrease long the channel in a similar manner to that displayed in figure 7(*a*). In both cases the waves vanish while still far from the beach. No measurements were performed in the monotonically decreasing region far from the wavemaker. It is important to stress here that distributions of type I represent wave regimes which are basically steady.

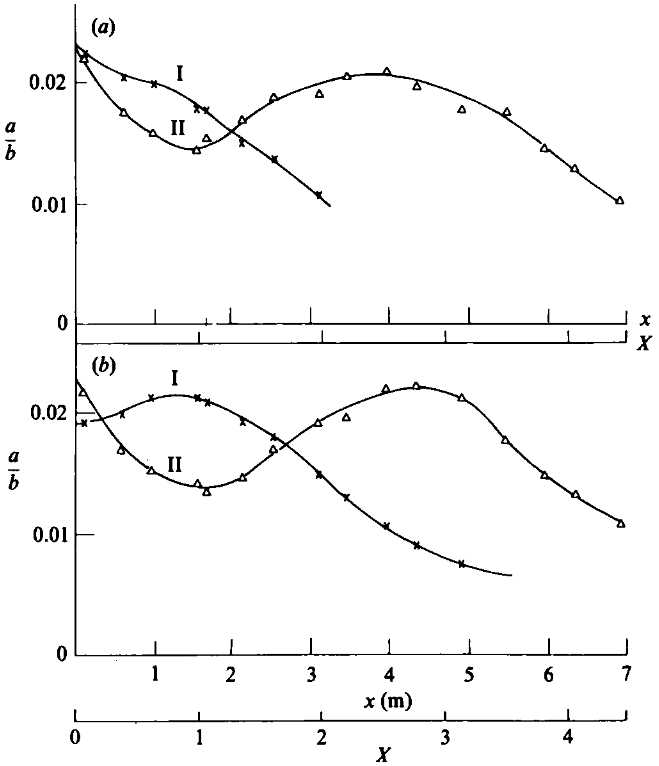

FIGURE 7. The distribution of wave amplitudes along the tank at (a) $kb/\pi = 1.9900, \lambda = -0.67$ and (b) $kb/\pi = 1.9913, \lambda = -0.58$; $\epsilon = 0.60 \times 10^{-4}$; ×, steady regime; △, unsteady regime.

The 'decaying' mode in the vicinity of the transition is different in essence from the linear solution and may be considered as a trapped soliton, discussed by Miles (1985). The presence of a trapped soliton may also explain the shift in the location of the maximum amplitude away from the wavemaker. A similar phenomenon was also observed in the cross-waves experiments reported by Barnard & Pritchard (1972) and Lichter & Shemer (1986).

In contrast with regime I, the family of curves labelled as II ('radiating' mode) represent essentially an unsteady wave field, which is characterized by modulation on a slow timescale. Before dealing with the details of the long time modulation, we shall restrict our analysis to values obtained from phase-averaging the results over times longer than the typical modulation period. The distinct property of a type II distribution shown in figure 7, is that the amplitude first decreases significantly, attains a minimum at a distance which is comparable with the width of the tank (and hence with the wavelength), and then increases again reaching a maximum at a substantial distance from the wavemaker. From that location on, the wave amplitudes decay monotonically towards the beach.

Although the phase hysteresis at a distance of 11 cm from the wavemaker is clearly seen in the experiment, the amplitude measurements at this location do not give a clear picture. The reason for that can be understood from a close scrutiny of the amplitude distributions shown in figure 7. One can see that close to the wavemaker the absolute difference in the wave amplitude between the 'decaying' and the 'radiating' modes is small. Moreover, the sign of this difference changes in a narrow

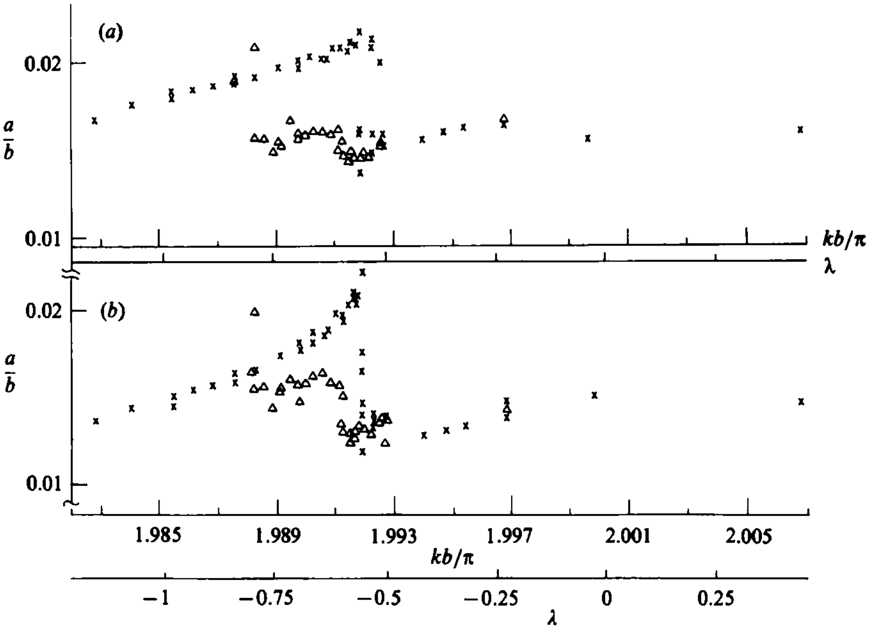

FIGURE 8. The dependence of wave amplitude (*a*) at $x = 111$ cm; $X = 0.834$ and (*b*) at $x = 160$ cm; $X = 1.20$, on wavenumber. ×, results for increasing frequency; △, decreasing frequency; amplitude of forcing $\epsilon = 0.60 \times 10^{-4}$.

range of frequencies. For this reason it is more instructive at the present stage to demonstrate the behaviour of the amplitudes in the vicinity of the transition at some distance from the wavemaker.

In figure 8 the dependence of wave amplitudes on the wavenumber is shown at a distance of 111 cm (figure 8*a*) and 160 cm (figure 8*b*) from the wavemaker. A well-defined hysteresis loop can be seen in both cases. In figure 8(*a*) the amplitude of the 'decaying' mode is always higher than that of the 'radiating' mode. In figure 8(*b*), on the other hand, the backward transition from the 'radiating' to the 'decaying' mode occurs practically without any amplitude change, and the hysteresis loop has the form of a triangle. The explanation for such a form may be again obtained from figure 7. One can see that there exists a crossing point between the amplitude distributions in the two modes; the location of the point where the amplitudes of both modes are equal moves closer to the wavemaker with decreasing frequency. At $kb/\pi = 1.987$ ($\lambda = -0.87$), this point is apparently located at a distance of about 160 cm from the wavemaker. At more distant locations, the amplitude will increase when a transition from the 'decaying' to the 'radiating' regime occurs. This may explain the difference between our results and the amplitude dependence on frequency, given by BMP, (see their figure 5).

5.4. *Long time modulation of the wave field*

Special attention was also paid to the detailed analysis of the unsteady behaviour of the wave field in the 'radiating' mode. The general view of the wave field at strong forcing is shown in figure 9. One can see that at the moment shown, the standing wave in the channel has a very pronounced 'hump' far from the wavemaker. This 'hump' is generated periodically at the wavemaker, and then moves slowly downstream and

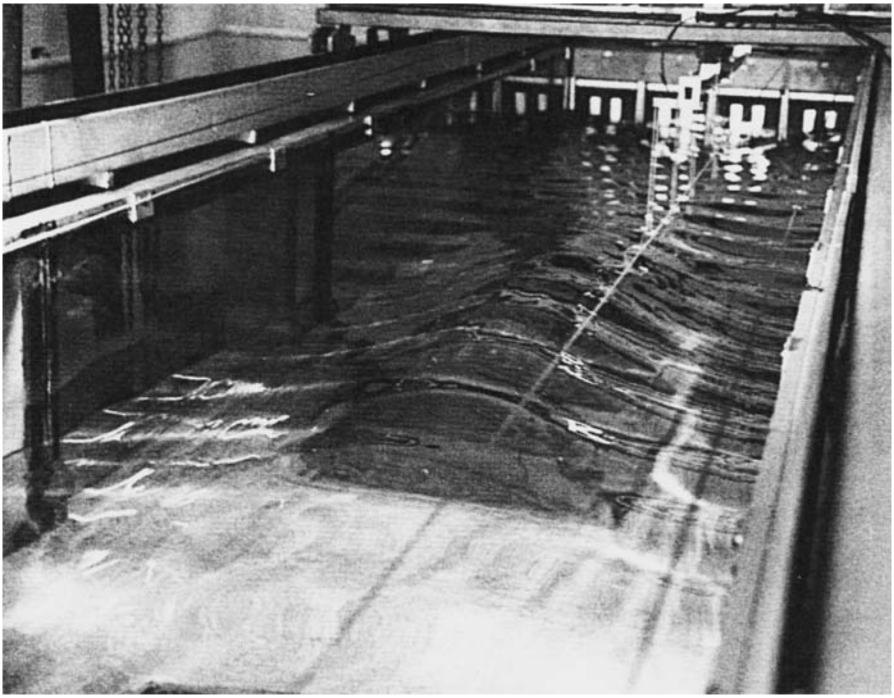

FIGURE 9. General view of the sloshing wave field at strong forcing.

decays far away. The extension of this structure along the channel is about 4 m. This 'hump' can be identified as an envelope soliton obtained in the numerical solution. The periodic behaviour at long timescale seems to be an additional display of Fermi–Pasta–Ulam recurrence phenomenon in water waves, as discussed theoretically by Yuen & Ferguson (1978*a*, *b*), Stiassnie & Shemer (1987) and Cox & Mortell (1986) and observed experimentally by Su & Green (1984) in Stokes waves and by Lichter & Shemer (1986) in cross-waves.

Since the unsteady character of the wave field is more pronounced at higher amplitudes of forcing, the data for $\epsilon = 0.83 \times 10^{-4}$ is presented first. The time dependence of the wave amplitudes measured simultaneously by four wave gauges, which are fixed to the probe carriage, are presented in figure 10. These measurements cover the range of wave-gauge locations from 11 cm to 9 m from the wavemaker (with X varying from 0.083 to 6.8), corresponding to 5 different carriage positions and for a total duration of 2114 s, or 2400 wave periods ($\tau \approx 78$).

The existence of a well-defined periodicity on the long timescale for all locations is evident. The period of the slow amplitude modulation is about 495 s ($\tau \approx 18$). The periodic modulation observed everywhere in the tank, is supplemented by a clear envelope soliton-type waveform which is developed at $x > 2$ m. The soliton propagation velocity (estimated from the measured shift in the position of the maximum amplitude at different probes), is about 4 cm/s (corresponding to dimensionless $X/\tau \approx 0.80$). One can also see from figure 10(*a*) that close to the wavemaker the modulation is relatively weak and it becomes more pronounced with increasing x. The increase in the modulation depth (ratio between maximum and minimum amplitudes) is accompanied by a growth in the maximum wave amplitude, which at

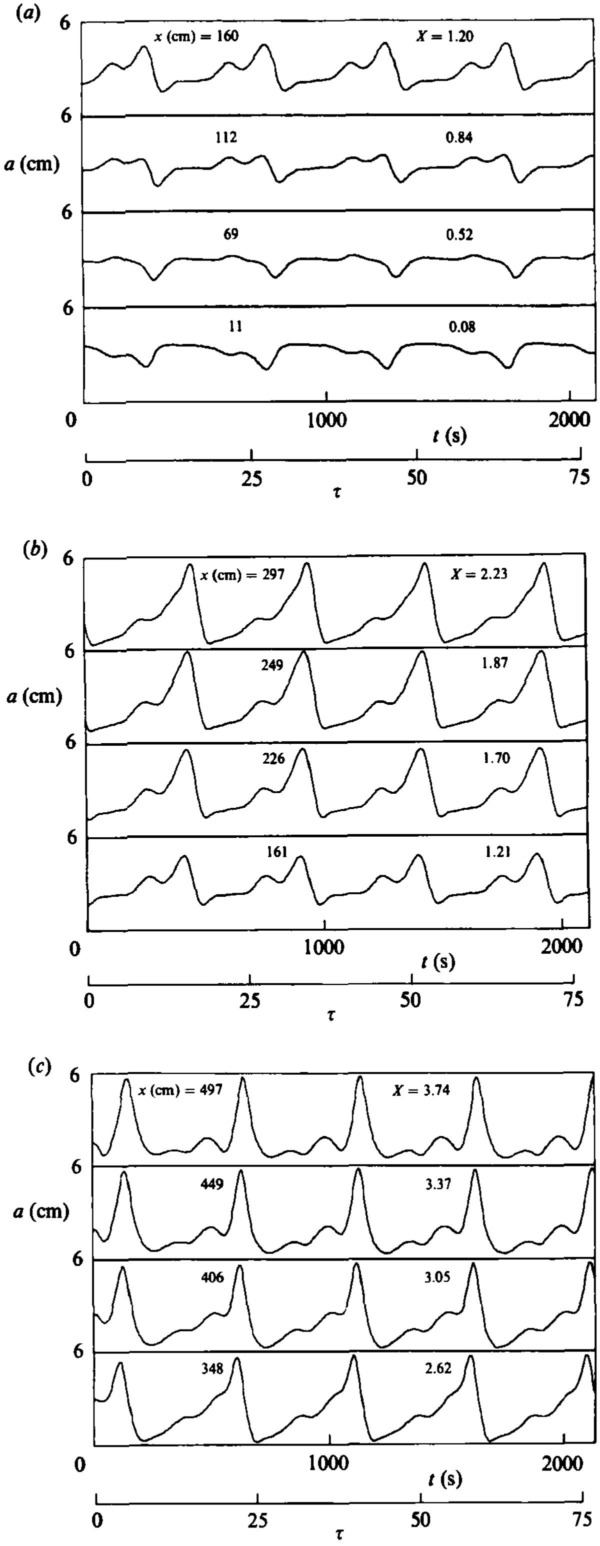

FIGURE 10(*a–c*). For caption see facing page.

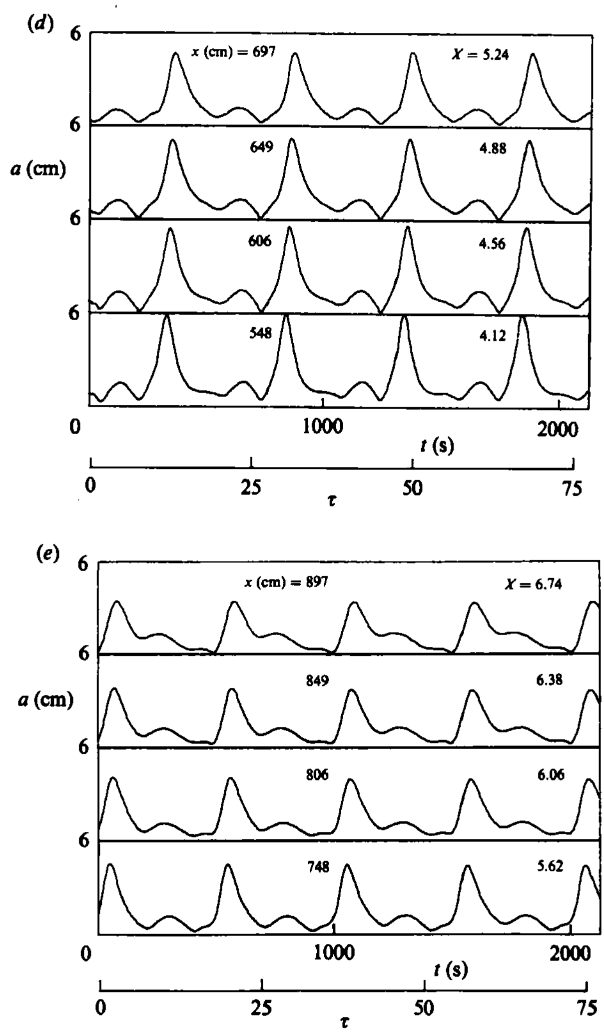

FIGURE 10. The dependence of sloshing wave amplitude on time at different locations along the channel for $\epsilon = 0.83 \times 10^{-4}$.

$x > 2$ m becomes nearly twice as large as the value in the vicinity of the wavemaker. At $x > 5$ m the wavy disturbance in front of the soliton nearly vanishes, and the wave amplitude differs notably from zero and only when the soliton is present.

One can assume that the increase in the height of the envelope soliton results from extracting energy from the background wave field. When the waves leading the soliton gradually disappear, the soliton height remains nearly constant ($2.5 \text{ m} < x < 5.5 \text{ m}$). For larger x, the soliton height decreases and this process is accompanied by a transfer of energy to background waves trailing the soliton (figure 10*e*, $x = 897$ cm). The total wave-energy decay rate along the channel is obviously due to dissipation (on the boundaries as well as in the bulk).

It is quite surprising to realize that at lower forcing amplitude, $\epsilon = 0.60 \times 10^{-4}$, the modulation period measured from figure 11, is about 505 s which is nearly the same as the absolute value measured at significantly higher amplitude. The renormalized dimensionless period now is about 13. At this lower forcing amplitude range no clear

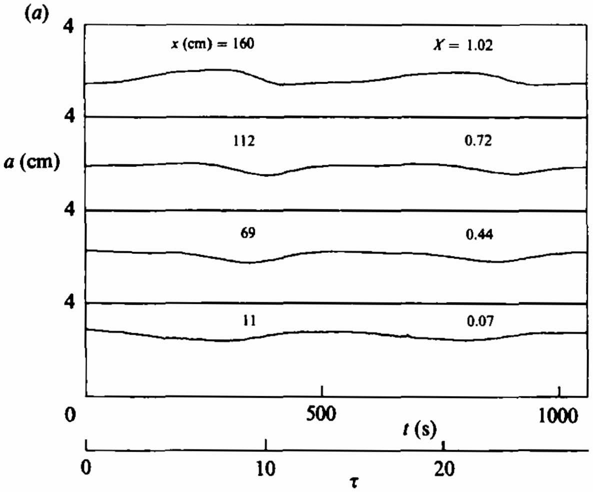

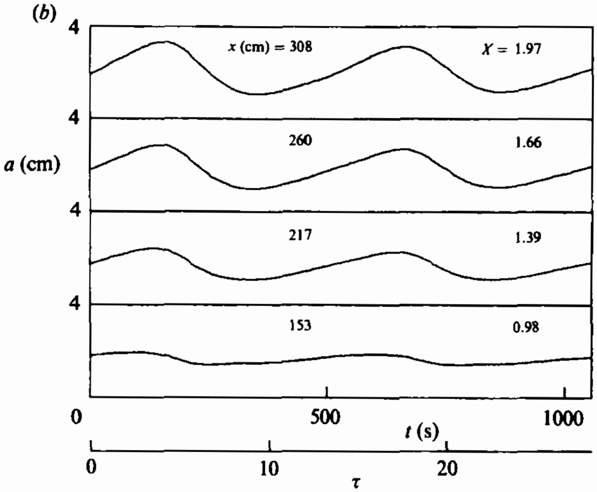

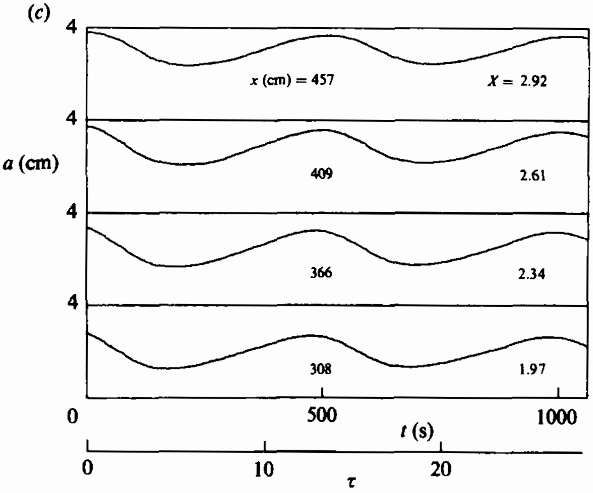

FIGURE 11. Same as in figure 11; $\epsilon = 0.60 \times 10^{-4}$.

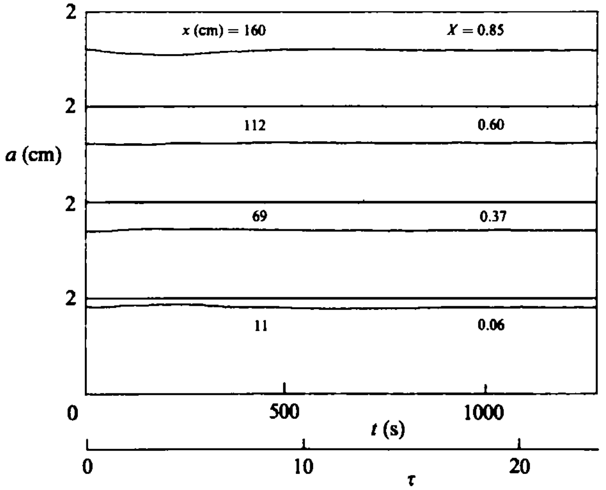

FIGURE 12. Same as in figure 11; $\epsilon = 0.42 \times 10^{-4}$.

soliton-like waveforms could be observed, but the general pattern of the maximum amplitude variation with x is quite similar to the strong forcing case. At even lower forcing, the modulation is extremely weak and could hardly be detected (figure 12), for this reason no clear conclusions regarding the modulation period could be drawn.

6. Discussion

The numerical solutions presented in §3 differ qualitatively from the experimental observations in three main aspects (i) in contrast with the numerical results, which gave a single propagating solition (see figure 1), the solitons observed in the experiments in the 'radiating' mode were generated periodically at the wavemaker; (ii) in the numerical solutions the wave amplitude at the wavemaker was found to be much higher than in the rest of the wavefield (figure 1), while in the experiments a quite different pattern was obtained (see figures 10 and 11); (iii) steady regimes were observed experimentally in the 'decaying' mode, but no such solutions were obtained numerically.

The NLS equation (2.39) includes a single tunable parameter λ, which represents the ratio between the detuning $(\Omega - \omega_2)$ and the forcing amplitude ϵ (see (2.40)). The normalized wave amplitude at the wavemaker $C_0(\tau) = |C(0, \tau)|$, shown in figure 2, depends therefore on λ and τ only, and is independent of the forcing ϵ. It thus seems interesting to compare the wave amplitudes measured experimentally at different forcing amplitudes in the vicinity of the wavemaker, with the numerically calculated values. Experimentally obtained amplitudes were calculated from the phase-averaged over long-time results. It thus appears reasonable to represent the numerically obtained oscillating quantities by some averaged values. Since the steady state in $C_0(\lambda, \tau)$ is never attained, it was arbitrarily decided that the mean value of the last period of oscillations at $\tau = 25$ (see figure 2) will be chosen as the representative amplitude. The amplitude C_0 is related to the dimensional wave amplitude a by

$$C_0 = \frac{a}{2b}\epsilon^{-\frac{1}{2}}. \tag{6.1}$$

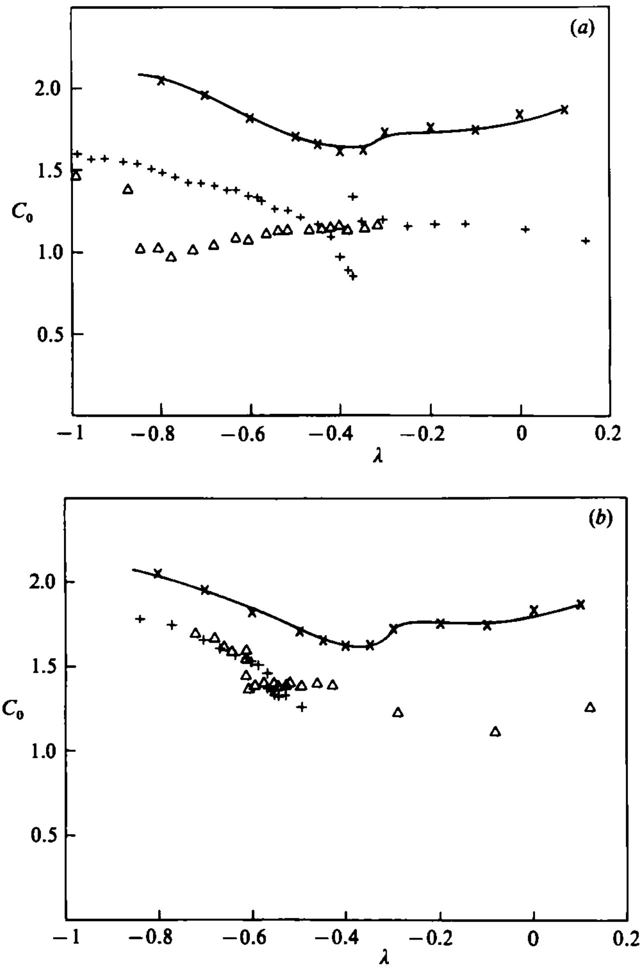

FIGURE 13. ×, the calculated normalized wave amplitudes at the wavemaker, as a function of the detuning parameter λ, compared to the experimentally obtained values (+, increasing frequency; △, decreasing frequency); (a) $\epsilon = 0.42 \times 10^{-4}$, (b) $\epsilon = 0.83 \times 10^{-4}$.

In figure 13 the numerically obtained wave amplitudes at the wavemaker are plotted as the function of λ and compared against the experimentally measured values, normalized according to (6.1), for $\epsilon = 0.42 \times 10^{-4}$ (figure 13a) and $\epsilon = 0.83 \times 10^{-4}$ (figure 13b). One can see that the agreement is quite reasonable in both cases, and it improves with increasing amplitude of forcing. The better agreement between theory and experiment at higher amplitudes of forcing manifests itself in two ways (i) the absolute normalized values of wave amplitude are slightly higher at larger ϵ, but are still below the theoretical curve; (ii) there is no hysteresis in the theoretical solution, and the transition from the 'decaying' to the 'radiating' mode seems to correspond to the minimum of the curve $C_0(\lambda)$, which ocurs at $\lambda \approx -0.4$. The experimentally observed transition occurs at the values of λ which are in quite good agreement with the theoretical prediction. The 'shrinking' of the hysteresis loop with increasing ϵ also indicates an improved agreement with the theory in this case.

Re-examination of figures 4 and 5 leads to similar conclusions. The hysteresis loops in figure 4 correspond to the values of the detuning parameter λ in the range $0.87 < \lambda < -0.37$ for $\epsilon = 0.42 \times 10^{-4}$; $-0.83 < \lambda < -0.54$ for $\epsilon = 0.60 \times 10^{-4}$ and $-0.61 < \lambda < -0.55$ for $\epsilon = 0.83 \times 10^{-4}$. The range of λ for which hysteresis is observed becomes therefore substantially narrower with stronger forcing. In figure 5, at the lowest frequency the transition occurs at strong forcing ($1.04 < \epsilon < 1.12$). These values of ϵ correspond to the range of variation of λ from -0.51 to -0.47, which is in good agreement with the theoretical curve of figure 13. At higher forcing frequency in figure 5, the hysteresis loop becomes wider (transition region $0.48 < \epsilon < 0.92$; $-0.84 < \lambda < -0.44$). At highest frequency, corresponding to $kb/\pi = 1.995$, the hysteresis loop shrinks again, $0.5 < \epsilon < 0.64$; $-0.40 < \lambda < -0.31$.

These results confirm the conclusion made in §5 that the inviscid model is, in principle, incapable of describing correctly all wave-field features which are observed experimentally. The essential role of dissipation was also stressed by Cox & Mortell (1986) in their numerical solution of the forced Korteweg–de Vries equation. In order to get a better qualitative agreement between experiment and theory, it seems therefore important to include dissipation effects in some way. Dissipation on the channel walls is a dominant mechanism in a real system (Ursell 1952) and should be included in the analysis. In most investigations, e.g. Ursell, BMP, which deal with a relatively deep channel, only dissipation on the sidewalls is considered. The numerical results, yielding extremely high amplitudes at $X = 0$, indicate, however, that dissipation at the wavemaker cannot be disregarded in our case.

In the present work we do not attempt to give a full solution of the dissipation problem, but rather try to incorporate some crude dissipation models in the NLS equation and in the boundary conditions. It is well known that viscous dissipation in any oscillatory flow occurs in the Stokes layer, which in our case has the width, see e.g. Schlichting (1975),

$$\delta_{\mathrm{St}} = (2\nu/\Omega)^{\frac{1}{2}} \approx 0.5\ \mathrm{mm} \ll b. \tag{6.2}$$

The phase shift between the potential flow velocity and the shear stress on the wall, is 45°. On the basis of these simple considerations we adopt the heuristic form similar to the one used by BMP to model the effect of dissipation on the walls and add to (2.39) a term $a_1(1+\mathrm{i})\,C$, where a_1 is some real positive number. In order to account for dissipation at the wavemaker, the boundary condition (2.41) is modified in the following way:

$$\frac{\partial C}{\partial X} + a_2(1+\mathrm{i})\,C = -\mathrm{i}, \tag{6.3}$$

where again a_2 is some positive number. The solution of the modified equation (2.39) with the wavemaker boundary condition (6.3) for $a_1 = 0$ (no sidewall dissipation) and $a_2 = 0.1$ (dissipation on wavemaker) is given in figure 14(*a*). One can immediately see that adding effective dissipation at the wavemaker, results in a dramatic change in the wave field. The periodic generation of solitons at the wavemaker can now be clearly seen. These periodically generated solitons propagate with the same velocity as the single soliton shown in figure 1(*a*). The numerical results displayed in figure 1(*a*) now resemble strongly the experimental observations.

The width of the soliton in figure 14(*a*) does not differ notably from that displayed in figure 1, and is about 4 dimensionless length units. This value is in good agreement

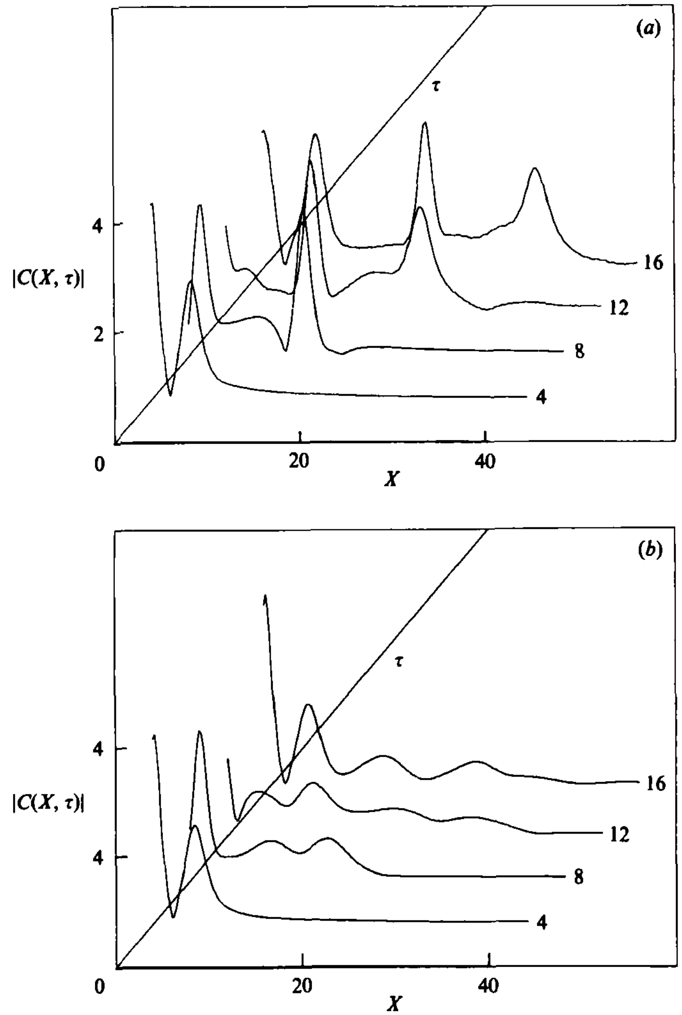

FIGURE 14. Space–time evolution of $|C(X, T)|$ for the dissipative model $\lambda = -0.1$; (a) $a_1 = 0$; $a_2 = 0.1$; (b) $a_1 = 0.1$; $a_2 = 0$.

with the soliton extension estimated from the experimental data presented in figures 9 and 10.

In figure 14(b) an attempt was made to take into account the sidewall dissipation ($a_1 = 0.1$) while neglecting the dissipation on the wavemaker ($a_2 = 0$). Here again, periodic generation of solitons is noticed. However, the solitons thus generated disappear very fast in the course of their motion down the channel due to strong dissipation.

Figure 15 displays the time evolution of the wave amplitudes at 4 locations, calculated for the parameters of figure 14(a), and provides an opportunity to compare directly the numerical results of the wavemaker dissipation model and the experimental data of figure 10.

The calculated wave amplitude at the wavemaker is now strongly reduced relative to the inviscid case and is much closer to the experimentally obtained values. Its time dependence is, however, still quite different from the one shown in figure 10(a), and

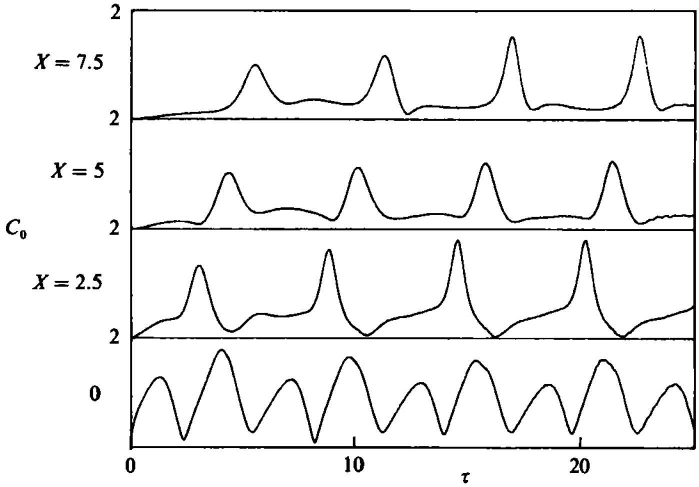

FIGURE 15. Wave amplitude time evolution at 4 locations along the channel for the data of figure 14(*a*).

qualitatively resembles the results obtained without dissipation at the wavemaker (compare with figure 2). The frequency of amplitude oscillations in figure 15 at $X = 0$ is somewhat different from the identical case without dissipation. It is interesting to note that this oscillation frequency is now twice the frequency of the appearance of the solitons.

For $X \geqslant 2$ the shape of the propagating soliton in figure 15 is quite similar to the one obtained experimentally. The non-dimensional soliton propagation velocity (about 2) is still substantially higher than that experimentally observed. The modulation period ($\Delta\tau \approx 6$) is also notably shorter than the one obtained from figures 7 and 8. We could not expect better quantitative agreement from the present simplified dissipation model. The disagreement, however, clearly indicates that the experimental results are strongly influenced by dissipation. The weakening of the modulation with decreasing amplitude of forcing, and the corresponding growth in the dimensionless value of the modulation period also support this conclusion.

All these facts indicate again that the inviscid nonlinear Schrödinger equation provides a better prediction of experimental observations at strong forcing. This can also be understood when one realizes that the relative importance of nonlinearity, as compared with essentially linear dissipation effects, increases with amplitude. The inviscid approach is thus more justifiable at higher wave amplitudes, where one can expect better quantitative agreement with experiment. The results of Lichter & Shemer (1986) for the cross-waves, where much higher soliton propagation velocities were recorded, seem to substantiate this conjecture.

Nevertheless, the inviscid solution still differs from the observations even for the highest amplitude employed in the present experiments. For example, the periodicity of soliton formation cannot be explained within the framework of inviscid theory. The very crude dissipation model incorporated both in the Schrödinger equation and in the boundary condition on the wavemaker, yields a qualitative agreement with high amplitude observations, and exhibits a periodic appearance of solitons. As a matter of fact, including dissipation in the model introduces an additional tunable parameter and effectively decouples frequency detuning and amplitude. A refined dissipation model will hopefully give even better agreement with the experiment, in particular at lower amplitudes of forcing.

These considerations can help us to understand the differences between the experimental results of BMP and those reported here. Since the wave tank used by BMP was narrower by a factor of 4 than our flume, the effective dissipation in their experiments was much stronger. That might be the reason why BMP did not report on any propagating solitons and on the existence of a long time modulation in their experimental work. From the results presented by BMP one can deduce, however, that a hysteresis phenomenon similar in nature to the one discussed in our work, was also present in their experiments. One can speculate that the reason for this hysteresis stems from a strong interaction between dissipation and nonlinear effects.

7. Conclusions

(i) A well-defined hysteresis phenomenon by amplitude or frequency was observed experimentally at the vicinity of the cutoff frequency, in a relatively narrow frequency band. The observation of the hysteresis loop was made possibly only owing to the fact that the operation of the wavemaker was extremely stable, with the possibility of very fine frequency tuning.

(ii) Two distinct wave regimes at identical forcing, depending on previous history and on frequency, were observed in the channel for all wavemaker amplitudes.

(iii) At relatively low forcing amplitude the observed wave field was essentially steady. Increasing the forcing results in an amplitude modulation on a long timescale. At highest forcing amplitude, solitons could be generated periodically at the wavemaker and then propagated down the channel with constant speed.

(iv) A cubic Schrödinger equation, valid for a semi-infinite rectangular channel filled to an arbitrary water depth and with a proper boundary condition at the wavemaker, was derived.

(v) The numerical solutions of this NLS equation were checked against experimental observations. Quantitative comparison of soliton propagation velocity, soliton width and location of transition, showed reasonably good agreement. This agreement improved significantly with increasing amplitude of forcing.

(vi) The inviscid NLS equation was found inadequate in explaining the periodicity of soliton generation at the wavemaker and the direct amplitude dependence of the observed wave field. The NLS equation and the boundary conditions on the wavemaker were therefore modified to incorporate, in a qualitative manner, the effect of dissipation.

(vii) The numerical solution of the modified nonlinear Schrödinger equation gave periodic appearance of propagating solitons similar to those observed in the experiments.

REFERENCES

Aranha, J. A., Yue, D. K. P. & Mei, C. C. 1982 Nonlinear waves near a cut-off frequency in an acoustic duct – a numerical study. *J. Fluid Mech.* **121**, 465–485.

Barnard, B. J. S., Mahony, J. J. & Pritchard, W. G. 1977 The excitation of surface waves near a cut-off frequency. *Phil. Trans. R. Soc. Lond.* A **286**, 87–123.

Barnard, B. J. S. & Pritchard, W. G. 1972 Cross-waves. Part 2. Experiments. *J. Fluid Mech.* **55**, 245–255.

Cox, E. A. & Mortell, M. P. 1986 The evolution of resonant water-wave oscillations. *J. Fluid Mech.* **162**, 99–116.

Garrett, C. J. R. 1970 On cross-waves. *J. Fluid Mech.* **41**, 837–849.

Larraza, A. & Putterman, S. 1984 Theory of non-propagating surface-wave solitons. *J. Fluid Mech.* **148**, 443–449.

Lichter, S. & Shemer, L. 1986 Experiments on nonlinear cross waves. *Phys. Fluids* **29**, 3971–3975.

Miles, J. W. 1976 Nonlinear surface waves in closed basins. *J. Fluid Mech.* **75**, 419–448.

Miles, J. W. 1984 Parametrically excited solitary waves. *J. Fluid Mech.* **148**, 451–460.

Miles, J. W. 1985 Note on parametrically excited trapped cross-wave. *J. Fluid Mech.* **151**, 391–394.

Miloh, T. 1987 Weakly nonlinear resonant waves generated by an oscillatory pressure distribution in a channel. *Wave Motion* **9**, 1–17.

Newman, J. N. 1977 *Marine Hydrodynamics*, pp. 247–248. MIT Press.

Penney, W. G. & Price, H. T. 1952 Part II. Finite periodic stationary gravity waves in a perfect fluid. *Phil. Trans. R. Soc. Lond.* A **244**, 254–284.

Schlichting, H. 1975 *Boundary Layer Theory*. McGraw-Hill.

Shemer, L., Kit, E. & Miloh, T. 1987 Measurements of two- and three-dimensional waves in a channel, including the vicinity of cut-off frequencies. *Expt Fluids* **5**, 66–72.

Stakgold, L. 1979 *Green's Function and Boundary Value Problems*, pp. 207–214. J. Wiley.

Stiassnie, M. & Kroszynski, U. I. 1982 Long-time evolution of an unstable water-wave train. *J. Fluid Mech.* **116**, 207–225.

Stiassnie, M. & Shemer, L. 1987 Energy computations for evolution of class I and II instabilities of Stokes waves. *J. Fluid Mech.* **174**, 299–312.

Su, M.-Y. & Green, A. W. 1984 Coupled two- and three-dimensional instabilities of surface gravity waves. *Phys. Fluids* **27**, 2595–2597.

Tadjbakhsh, L. & Keller, J. B. 1960 Standing surface waves of finite amplitude. *J. Fluid Mech.* **8**, 442–451.

Ursell, F. 1952 Edge waves on a sloping beach. *Proc. R. Soc. Lond.* A **214**, 79–97.

Wehausen, J. V. 1974 Methods for boundary-value problems in free-surface flows. *The Third D. W. Taylor Lecture, DTNSRDC Rep.* 4622. Bethesda, Maryland.

Wu, J., Keolian, R. & Rudnick, I. 1984 Observation of a nonpropagating hydrodynamic soliton. *Phys. Rev. Lett.* **52**, 1421–1424.

Yuen, H. C. & Ferguson, W. E. 1978*a* Relationship between Benjamin–Feir instability and recurrence in the nonlinear Schrödinger equation. *Phys. Fluids* **21**, 1275–1278.

Yuen, H. C. & Ferguson, W. E. 1978*b* Fermi–Pasta–Ulam recurrence in the two-space dimensional nonlinear Schrödinger equation. *Phys. Fluids* **21**, 2116–2118.